Journal of Alloys and Compounds 784 (2019) 1106–1112

Contents lists available at ScienceDirect

Journal of Alloys and Compounds

journal homepage: http://www.elsevier.com/locate/jalcom

Effects of laser surface alloying with Cr on microstructure and hardness of commercial purity Zr

Ke Chen [a], Lingguo Zeng [b], Zhijun Li [b], Linjiang Chai [a, *], Yueyuan Wang [a], Liang-Yu Chen [c], Hailiang Yu [d, **]

[a] College of Materials Science and Engineering, Chongqing University of Technology, Chongqing 400054, China
[b] Chongqing Yufeng Wire and Cable Co., Ltd, Chongqing 402260, China
[c] School of Science, Jiangsu University of Science and Technology, Zhenjiang, Jiangsu 212003, China
[d] College of Mechanical and Electrical Engineering, Central South University, Changsha 410083, China

ARTICLE INFO

Article history:
Received 26 November 2018
Accepted 8 January 2019
Available online 9 January 2019

Keywords:
Zr
Laser surface alloying
Microstructure
Hardness
Electron backscatter diffraction

ABSTRACT

Pulsed laser was utilized to treat a commercial purity Zr (CP Zr) sheet coated with Cr by brush plating to achieve Cr alloying on its surface. Microstructural characteristics and hardness of the laser-treated surface were investigated by use of electron channeling contrast imaging, electron backscatter diffraction, energy dispersive spectrometry techniques and microhardness measurement. Results show that after the laser surface alloying (LSA) with Cr, five zones with distinctly different microstructural characteristics are presented from the surface to the matrix: two melted zones (MZs), two solid-state phase transformation zones (SSPTZs) and the unchanged matrix. The MZ-1 and the MZ-2 are featured by equiaxed and columnar structures with internal substructures inside them, respectively. The SSPTZ-1 is fully comprised of martensitic plates transformed from complete β domains while the SSPTZ-2 contains both martensitic plates and bulk α grains due to cooling from α+β domains. The Cr alloying mainly occurs in the two melted zones (MZ-1 and MZ-2) while essentially not in the SSPTZs. Compared with the initial microstructure, many low angle boundaries appear in untransformed bulk α grains in the SSPTZ-2, which is related to thermal stresses induced by the laser surface treatment. Hardness measurements show that the LSA with Cr can effectively increase the surface hardness of the CP Zr, with the maximum value (468 HV) to be ~2.4 times that of the matrix. Such hardening could be mainly attributed to solid-solution strengthening of Cr in α-Zr and significant grain refinement.

1. Introduction

Excellent nuclear properties (especially low neutron absorption) and good mechanical properties have made Zirconium (Zr) alloys be extensively used in the nuclear industry for many years [1–4]. Most Zr alloys for the nuclear application are fabricated as pressure tubes and/or fuel claddings, with high surface properties needed for reliable work. However, wear- and corrosion-resistance of their surfaces are generally believed to be relatively limited and need to be considerably improved. To this end, many surface treatment techniques have been attempted to optimize the surface properties of various Zr alloys (e.g. Refs. [5–11]). Among them, laser surface treatment (LST) has been recognized to be a feasible and effective method, with several successful examples already reported. Amouzouvi et al. [12] treated a Zr-2.5Nb alloy by use of a continuous wave CO_2 laser and found that its hardness near surface could be significantly improved. More recently, Chai et al. [13–16] employed pulsed laser to treat surfaces of a few typical single-phase and dual-phase Zr alloys and noted that hardening was always the most effective in places close to the laser beam center, where the greatest microstructural refinement were found.

In addition to direct LST processing for bare alloys, it was found that laser surface alloying (LSA) was able to further improve surface corrosion- and wear-resistance of Zr alloys. Lee et al. [17] and Zhang et al. [18] reported that the surface hardness and the resistance to localized corrosion of Zircaloy-4 were significantly improved after LSA with Nb. Note that Cr is often regarded as an important alloying element of Zr alloys and its proper addition can lead to considerably

* Corresponding author.
** Corresponding author.
E-mail addresses: chailinjiang@cqut.edu.cn (L. Chai), yuhailiang@csu.edu.cn (H. Yu).

https://doi.org/10.1016/j.jallcom.2019.01.097
0925-8388/

enhanced corrosion-resistance and mechanical properties [19–21]. To date, however, very few attempts have been made to achieve surface alloying with Cr for Zr alloys. More specifically, in regards to LSA with Cr on Zr alloys, no results could be found in public literature despite its expected effectivity.

Therefore, in this study, a commercial purity zirconium (CP Zr) sheet was subjected to the LSA with Cr. Microstructural characteristics induced by the treatment were investigated by combined use of electron channeling contrast (ECC) imaging, electron backscatter diffraction (EBSD) techniques and energy dispersive spectroscopy (EDS). Hardnesses before and after the LSA were measured and correlated with the revealed microstructural characteristics to explore related surface modification mechanisms.

2. Experimental

The as-received material was a CP Zr sheet after cold rolling and recrystallization annealing, with few impurities of 1.15 wt.% Hf, 0.15 wt.% O and <0.1 wt.% Fe + Cr. Its transus temperatures for α, β and liquid phase were estimated to be ~800 °C, ~960 °C and ~1850 °C, respectively. A specimen with dimensions of 6, 7.5 and 2 mm along rolling, transverse and normal directions (denoted as RD, TD and ND, respectively) was cut from the as-received sheet. After careful cleaning, a thin layer of Cr was coated on the RD-TD surface of the specimen by brush plating at room temperature. Subsequently, a pulsed Nd: YAG laser device (HWLW-600A-C-V5.2.01) was utilized to treat the Cr-coated surface. The laser processing was conducted at a scanning speed of 8 mm/s along the TD with beam power of 200 W, energy density of 25 J/mm, beam diameter of 1 mm, defocusing amount of +2 mm, pulse width of 5 ms and pulse frequency of 20 Hz. During the laser processing, the irradiated zones were protected by a continuous flow of Ar gas to avoid oxidation.

Microstructures of the RD-ND plane of the LSAed specimen were mainly characterized by ECC imaging and EBSD techniques in a field emission gun scanning electron microscope (Zeiss Sigma HD). The EBSD system had a NordlysMax^2 detector (Oxford Instruments) with Aztec 2.4 and HKL Channel 5 software packages used for data acquisition and postprocessing, respectively. EDS was also employed to detect local compositions of the LSAed specimen. In addition, hardness measurements were performed on the RD-TD surface using a Vickers indentation tester (HVS-1000) at a load of 100 g for 10 s. The tester was able to accurately locate position (coordinate) of each indentation so that the hardness could be well correlated with specific microstructures. Prior to microstructural examinations and hardness measurements, the to-be-analyzed surfaces were first mechanically ground using SiC papers and then electro-polished in a mixed solution of 10 vol.% perchloric acid, 20 vol.% butyl cellosolve and 70 vol.% methanol at 20 V and −30 °C for 40 s.

3. Results and discussion

3.1. The un-LSAed specimen

Fig. 1a (ECC image) reveals that the microstructure of the as-received CP Zr is composed of typical equiaxed grains with a few randomly distributed second phase particles (SPPs). Such microstructural features have often been observed in rolled and fully recrystallized Zr alloys [22,23]. Average sizes of the grains and the SPPs are measured to be about 8.3 μm and 0.5 μm, respectively. Fig. 1b is an EBSD inverse pole figure (IPF) map with black and gray lines delineating high angle boundaries (HABs, $\theta > 15°$) and low angle boundaries (LABs, $2° < \theta < 15°$), respectively. According to the standard triangle (the inset in Fig. 1b), most of the grains in the IPF map are colored near red, suggesting their c-axes to be close to the ND of the sheet. A misorientation angle distribution histogram corresponding to Fig. 1b is presented in Fig. 1c, from which the majority of grain boundaries are seen to be HABs, confirming full recrystallization for the as-received material.

A cross-sectional view of CP Zr after brush plating Cr is presented in Fig. 2a, from which the Cr layer and the matrix can be clearly distinguished. The result of EDS line scanning along the arrowed path in Fig. 2a is shown in Fig. 2b. One can see that both the Zr matrix and the Cr coating are rather pure, with a relatively sharp compositional boundary between them. This indicates that no Cr alloying should have occurred for the Zr matrix during the brush plating. From both the microstructural observation and the composition measurement, the average thickness of the Cr coating is determined to be about 22 μm.

3.2. Microstructures of the LSAed specimen revealed by ECC

Fig. 3 presents cross-sectional observations (ECC images) and the EDS line scanning result of the LSAed specimen. From Fig. 3a (a low-magnification image), five zones with different microstructural characteristics can be distinguished, as roughly separated by dashed lines. There are two melting zones (MZ-1 and MZ-2), two solid-state phase transformation zones (SSPTZ-1 and SSPTZ-2) and the CP Zr matrix. The maximum width and depth of the laser-modified regions are measured to be ~1.5 mm and ~0.9 mm, respectively. The width and the depth of the MZ are ~1.0 mm and ~0.6 mm, respectively. A selected region B in Fig. 3a is magnified in Fig. 3b, revealing that the MZ-1 is composed of structures with equiaxed morphology. For the MZ-2, however, a closer observation reveals columnar structures with their length directions always towards the beam center. Note that both the equiaxed and the columnar structures should correspond to morphologies of the high-temperature β phase that is solidified from the liquid phase. During further cooling, the β phase in either equiaxed or columnar morphology would usually be transformed into fine α plates, with the prior β grain boundaries retained though. As for reasons accounting for the formation of equiaxed structures in the MZ-1 and columnar structures in the MZ-2, a brief analysis is as follows: during the solidification from liquid phase (L) to β, β nuclei usually prefer to grow along the direction with the largest temperature gradient. Since the laser beam will directly work on the MZ-1, sufficient heat allows melting to occur in this zone and adjacent regions with similar temperatures between them [24]. As a result, only small temperature gradients and limited anisotropic growth of β nuclei could be expected for the MZ-1, leading to the formation of the equiaxed β grains. In the MZ-2, the temperature of the melts near the beam center (MZ-1) is definitely higher than that near the matrix, producing an evident temperature gradient. Therefore, during solidification, the β nuclei have the highest growth rate along the direction with the maximum temperature gradient (towards the beam center) and eventually grow into columnar grains.

Fig. 3c presents a magnified observation for the region C in Fig. 3a, with parts of both the SSPTZs included. From Fig. 3c, one can see that the SSPTZ-1 is also comprised of coarse columnar structures (prior β grains) while the microstructure in the SSPTZ-2 is much finer than that in the matrix. The EDS line scanning result in Fig. 3d reveals that there exists a large amount of Cr in both the MZs, confirming that effective Cr alloying has been achieved by the pulsed laser surface treatment. Along the measuring path in Fig. 3d, the content of Cr is found to be decreased significantly in regions corresponding to the SSPTZ-1. Furthermore, hardly any Cr can be detected in the SSPTZ-2. This indicates that the Cr alloying is much less effective in the SSPTZs than in the MZs, which could be ascribed to limited diffusion of Cr in the SSPTZs with lower

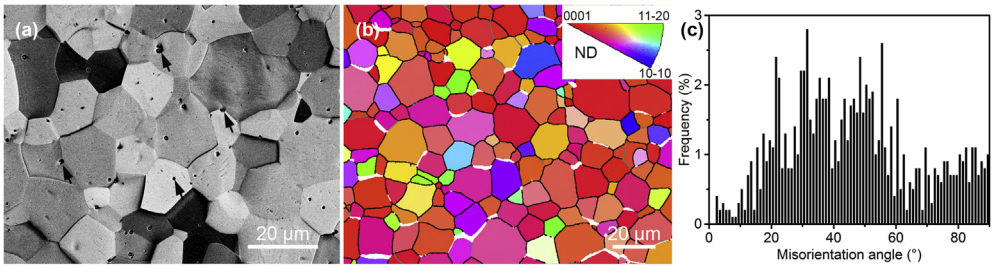

Fig. 1. Microstructural characteristics of the as-received specimen: (a) ECC image with black arrows indicating SPPs; (b) EBSD IPF map with black and gray lines representing HABs and LABs, respectively; (c) misorientation angle distribution histogram corresponding to (b).

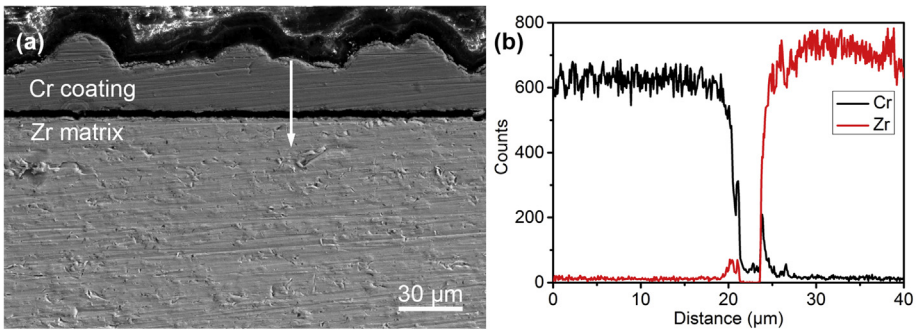

Fig. 2. (a) Cross-sectional view of the specimen after plating Cr; (b) EDS line scanning result along the arrowed path in (a).

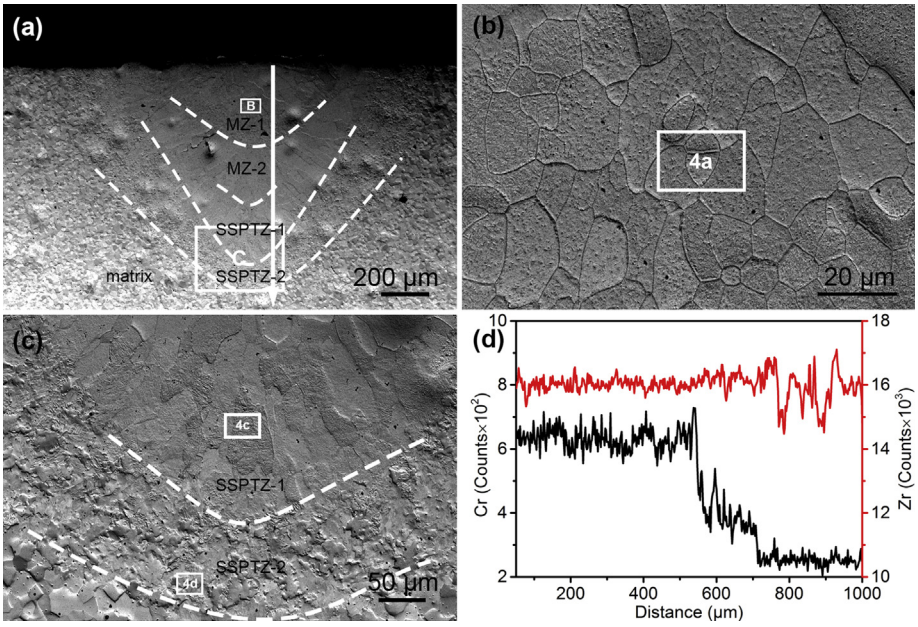

Fig. 3. ECC images of the LSAed specimen at different magnifications: (a) cross-sectional view of the laser-modified regions at low magnification; (b) magnified image corresponding to region B in (a); (c) magnified image corresponding to region C in (a); (d) EDS line scanning result along the arrowed path in (a).

temperatures.

Fig. 4 presents ECC observations of the LSAed specimen at high magnification. Fig. 4a is a magnified image corresponding to the boxed region 4a in Fig. 3b. It can be found that inside the equiaxed structures in the MZ-1, a large number of fine substructures exist and they probably correspond to ultra fine α plates. Similar substructures are also found in the columnar structures in the MZ-2 (Fig. 4b). Fig. 4c and d correspond to the boxed regions 4c and 4d in Fig. 3c, respectively. A number of plates in either parallel or interlaced morphology can be seen in the SSPTZ-1, with most of their widths at sub-micron level. They are believed to be the martensitic structures produced by rapid β→α cooling during the laser treatment [25]. A mixture of plate structures and bulk grains is noticed in Fig. 4d, suggesting that the SSPTZ-2 should have been cooled down from α+β domains, i.e., α+β→α transformation. The plates are transformed from the high temperature β phase while the bulk grains correspond to the prior α grains.

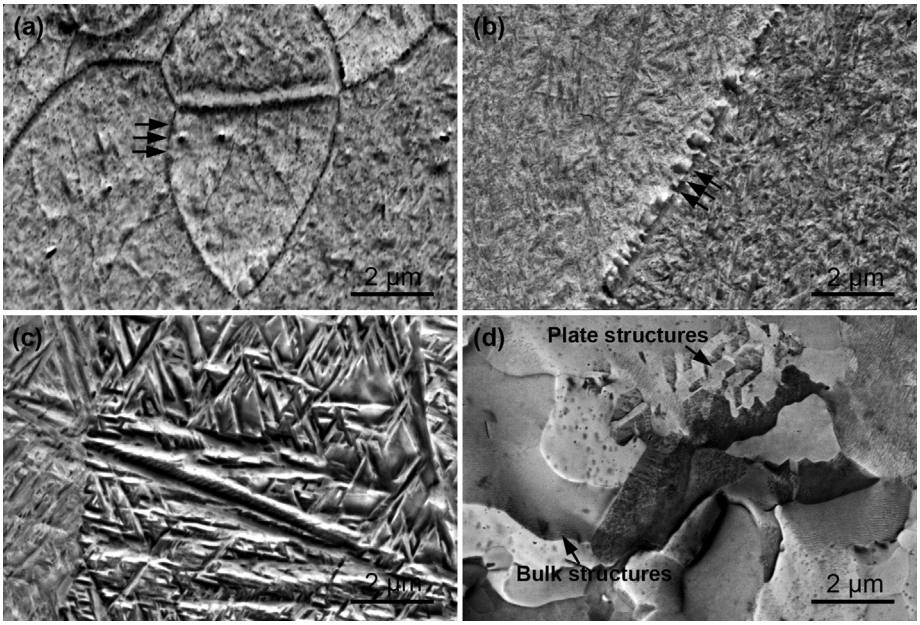

Fig. 4. ECC images of the LSAed specimen at high magnification: (a) MZ-1 (the boxed region 4a in Fig. 3b), (b) MZ-2, (c) SSPTZ-1 (the boxed region 4c in Fig. 3c) and (d) SSPTZ-2 (the boxed region 4d in Fig. 3c); arrows in (a) and (b) indicate boundaries of preexisting β phases.

3.3. Microstructures of the LSAed specimen revealed by EBSD

Fig. 5a and c presents EBSD band contrast maps of the MZ-1 and the MZ-2. Although their indexing rates are relatively low due probably to a rather high density of internal defects in both the MZs, equiaxed and columnar structures can still be observed, consistent with the morphological features revealed in Fig. 3. Fig. 5b and d shows that both the MZs have the same misorientation angle distribution characteristic, namely, the presence of three major peaks around 10°, 60° and 90°. For Zr alloys, according to the Burgers orientation relationship (OR) ($\{0001\}_\alpha//\{110\}_\beta$ and $<11\bar{2}0>_\alpha//<111>_\beta$) [26], there are five possible misorientations (10.5°/<0001>, 60°/<11−20>, 60.8°/~<12−31>, 63.3°/~<44−83> and 90°/~<12−30>) between any two α orientations generated by the same β parent. After careful comparisons, the misorientation characteristics presented in Fig. 5b and d are

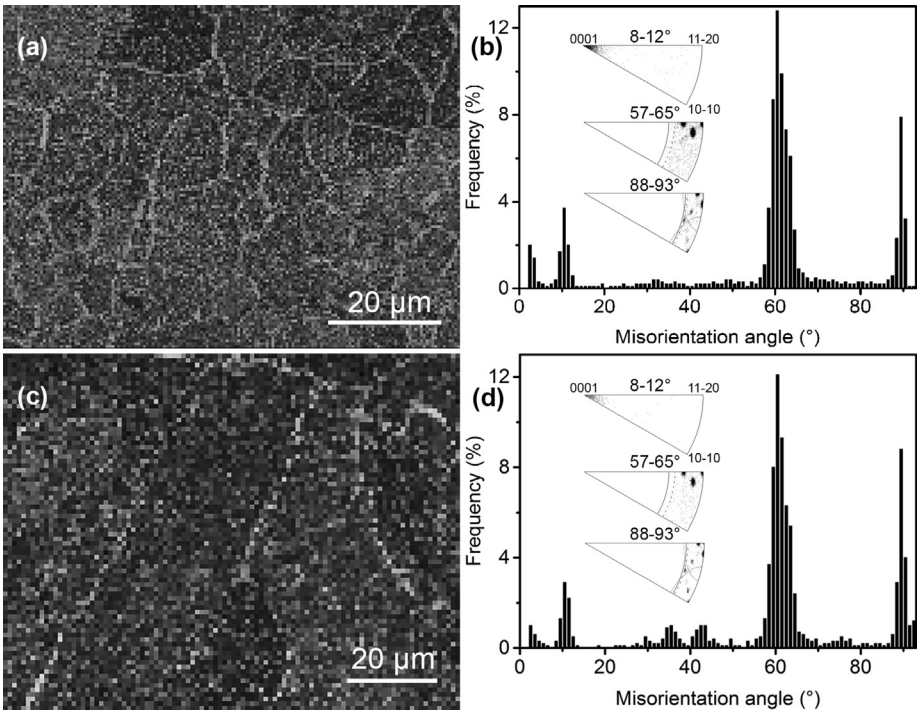

Fig. 5. (a) and (c) EBSD band contrast maps of MZ-1 and MZ-2, respectively; (b) and (d) misorientation angle and rotation axis distributions corresponding to (a) and (c), respectively.

confirmed to well coincide with those Burgers misorientations. It is thus known that relatively sufficient β→α phase transformation should have occurred in both the MZs.

The EBSD characterization results of both the SSPTZs are shown in Fig. 6. Fig. 6a is an EBSD band contrast map with dashed lines roughly distinguishing different zones, most of which are found to belong to the SSPTZ-2 (after the α+β→α transformation). An IPF map corresponding to Fig. 6a is presented in Fig. 6b, from which orientations of the plate structures in both the SSPTZ-1 and the SSPTZ-2 appear to be rather scattered. This is different from the case that most grains align their c-axes towards the ND in the matrix (Fig. 1). According to the Burgers OR [27], six different β orientations can be produced by one α orientation during heating and one β orientation is able to give birth to twelve different α orientations during cooling. In other words, 72 different α orientations can be generated from one initial α orientation after an α→β→α cycle. Therefore, during the laser surface treatment, a large number of new α orientations are expected to be produced by the α→β→α transformation, resulting in the scattered orientations of the plate structures. Fig. 6c and d are the misorientation angle and rotation axis distributions corresponding to Fig. 6a, respectively. It can be seen that misorientations of most grain boundaries in this region belong to the aforementioned Burgers misorientations, similar to the cases of both the MZs revealed in Fig. 5.

In addition, it is noticed from Fig. 6b that although those α grains in the SSPTZ-2 without phase transformation are still in bulk morphology, there are always many LABs in their interiors. This is different from the LABs-free case in the starting microstructure. One of such grains (as arrowed in Fig. 6b) are extracted and exemplarily analyzed in Fig. 7. Fig. 7a clearly shows that the grain is divided into several irregular-shaped subgrains by LABs, Moreover, Fig. 7b reveals that misorientation angles of these LABs are relatively low and focused on 3–5°, with their rotation axes exclusively concentrated on <0001>. In consideration of slip behaviors of hcp α-Zr, such misorientations could only be caused by prismatic slip of <a> dislocations [22,28]. Since the SSPTZ-2 is cooled from the α+β domains, thermal stresses associated with the formation of plate structures (martensites) are able to directly act on the neighboring bulk α grains. As a result, active dislocation movement and rearrangement could occur, eventually leading to the formation of the LABs in Fig. 7. In a recent study on an LSTed dual-phase Zr-2.5Nb alloy [13], it was found that such thermal stresses could be absorbed by soft β films that surround the untransformed α grains and thus almost no LABs are produced in their interiors, different from the case here.

3.4. Hardness variation

The hardness variation after the LSA with Cr is presented in Fig. 8. The surface hardness of the specimen is found to be relatively uniform for locations far from the laser beam center, which corresponds to the matrix with an average value of 195 HV. For locations near the beam center, however, significant hardness increase can be noticed, with the highest value of 468 HV which is ~140% higher than that of the matrix. This manifests that the CP Zr surface is able to be remarkably hardened by the LSA with Cr. Fig. 8 also shows that the width of hardened zones is ~1.0 mm which well agrees with that of the MZs as revealed in Fig. 3, suggesting their correspondence. Based on the above microstructural characterization made for the laser-modified zones, reasons for the hardness increase can be tentatively analyzed as follows.

Firstly, as verified in Fig. 3d, a considerable amount of Cr is introduced by the LSA treatment into the CP Zr, which may bring effective solid-solution strengthening/hardening. According to the Zr–Cr binary diagram [29], the maximum solubility of Cr in α-Zr is less than 0.5 at.%. However, EDS analyses show that the Cr content in the MZs of the LSAed specimen could be ~4.0 at.%, much higher than its solubility. As the cooling rates induced by the pulsed laser are rather high, diffusion behaviors of alloying elements tend to be suppressed during the phase transformation. As a result, the enriched Cr should mainly exist in the α-Zr as supersaturated elements. Yang et al. [30] reported that an increment of ~18.1 MPa in yield strength would be aroused by per 0.1 at.% Cr solid solution in α-Zr. Then, the total increment of yield strength caused by the Cr alloying in the present case would at most be ~724.0 MPa, approximately corresponding to a hardness increase of ~219.4 HV using the empirical equation of $\sigma_y \approx 3.3$ HV [23]. Secondly, the L→β→α transformation during the LST transforms the prior equiaxed grains into fine martensitic plates, which allow significant strengthening/hardening due to grain refinement to be expected. Although sizes of the transformed plates in the MZs are extremely small and hard to be measured accurately, they could be roughly estimated referring to the plate widths in the SSPTZs (~0.2 μm on average). Since Cr is a typical β-Zr stabilizer and can lower the starting temperature of martensitic transformation (M_s), more addition of Cr would produce finer martensitic plates during the β→α transformation [19]. Clearly, the Cr content in the MZs is higher than that in the SSPTZs, suggesting α-plate widths in the Cr-enriched zones to be < 0.2 μm. Such a value is greatly smaller than the average grain size of equiaxed grains (~8.3 μm) in the matrix and thus significant Hall-Petch hardening can be produced.

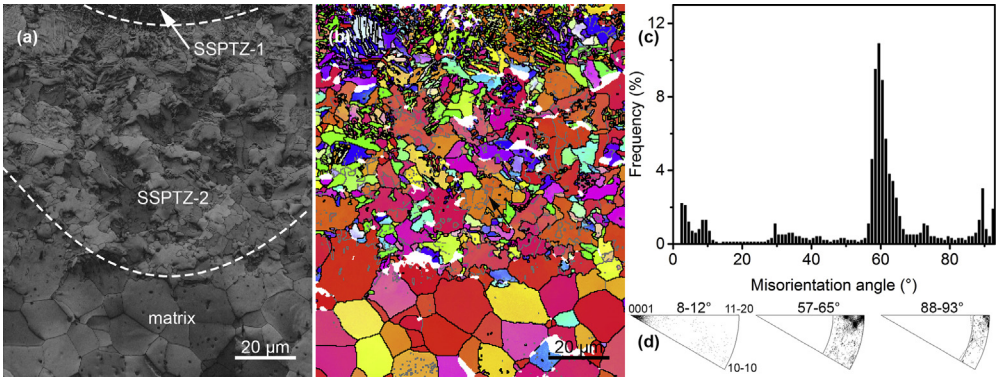

Fig. 6. (a) EBSD band contrast map corresponding to SSPTZ and matrix, respectively; (b) IPF map corresponding to (a); (c) misorientation angle distribution and (d) rotation axis distribution corresponding to (a). The color code in (b) is the same as that in Fig. 1b. (For interpretation of the references to color in this figure legend, the reader is referred to the Web version of this article.)

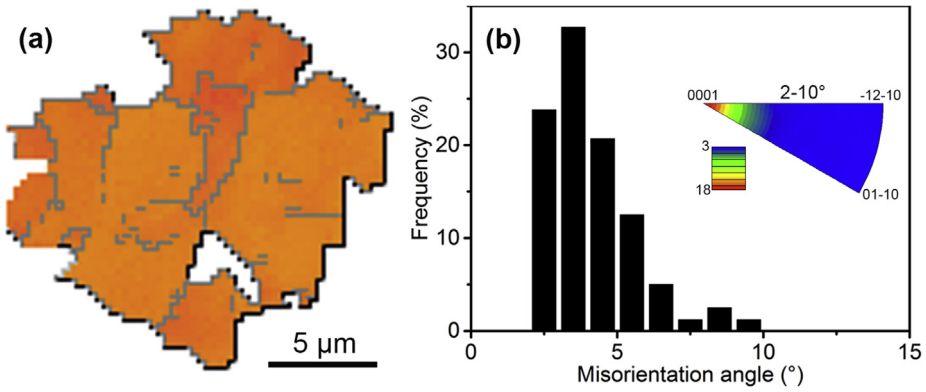

Fig. 7. (a) An extracted grain from the SSPTZ-2 in Fig. 6b (as indicated by the arrow); (b) misorientation angle and rotation axis distributions corresponding to (a).

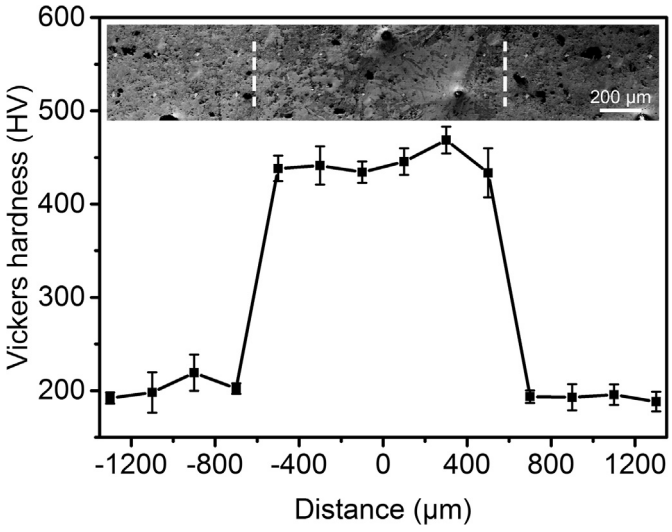

Fig. 8. Hardness variation across the laser-treated zones on the RD-TD surface; the horizontal coordinate indicates distances from the exact center of the laser beam. True morphologies and locations of the hardness indentations are also revealed in the inset micrograph with dashed lines roughly indicating interfaces between the matrix and the laser-modified zones.

Earlier work on an LSTed CP Zr without Cr alloying showed that hardness of laser-modified zones was ~80% higher than that of the matrix [14,31]. Besides, for a dual-phase Zr-2.5Nb, its surface hardness could be increased by ~70–90% after the LST without Cr alloying [13,32]. Comparatively, the LSA with Cr treatment in the present work could lead to much more effective surface hardening with the hardness increase of ~140%.

4. Conclusions

(1) After the LSA with Cr, four laser-modified zones with different microstructural characteristics are observed from the surface to the matrix: MZ-1, MZ-2, SSPTZ-1 and SSPTZ-2. The MZ-1 and the MZ-2 are featured by equiaxed and columnar structures with internal substructures, respectively. The SSPTZ-1 is fully comprised of martensitic plates transformed from complete β domains while the SSPTZ-2 contains both martensitic plates and bulk α grains due to cooling from α+β domains.

(2) The Cr alloying mainly occurs in the two melted zones (MZ-1 and MZ-2) while essentially not in the SSPTZs with only solid-state phase transformation.

(3) Compared with conventional laser surface treatments, the LSA with Cr is able to more effectively harden the surfaces of CP Zr and the maximum hardness is ~2.4 times that of the matrix, which could be mainly attributed to solid-solution strengthening of Cr in α-Zr and significant grain refinement.

Acknowledgments

This work is financed by the Fundamental and Cutting-Edge Research Plan of Chongqing (Nos. cstc2018jcyjAX0299 and cstc2017jcyjAX0114), the Education Reform Project for Professional Degree Graduate of Chongqing University of Technology (ZSSD103-2018CLCXCY1006) and the National Natural Science Foundation of China (51601075).

References

[1] Z. Duan, H. Yang, Y. Satoh, K. Murakami, S. Kano, Z. Zhao, J. Shen, H. Abe, Current status of materials development of nuclear fuel cladding tubes for light water reactors, Nucl. Eng. Des. 316 (2017) 131–150.
[2] S.J. Zinkle, G.S. Was, Materials challenges in nuclear energy, Acta Mater. 61 (2013) 735–758.
[3] L. Chen, Q. Zeng, J. Li, J. Lu, Y. Zhang, L. Zhang, X. Qin, W. Lu, L. Zhang, L. Wang, D. Zhang, Effect of microstructure on corrosion behavior of a Zr–Sn–Nb–Fe–Cu–O alloy, Mater. Des. 92 (2016) 888–896.
[4] Z.N. Yang, X.B. Wang, F. Liu, F.C. Zhang, L.J. Chai, R.S. Qiu, L.Y. Chen, Effect of intercritical annealing temperature on microstructure and mechanical properties of duplex Zr-2.5Nb alloy, J. Alloy. Comp. 776 (2019) 242–249.
[5] C. Tang, M. Stueber, H.J. Seifert, M. Steinbrueck, Protective coatings on zirconium-based alloys as accident-tolerant fuel (ATF) claddings, Corros. Rev. 35 (2017) 141–165.
[6] S. Yang, Z. Guo, M. Zhang, Q. Guan, Y. Jin, Y. Liu, Effect of high current pulsed electron beam surface irradiation on the microstructure and electrochemical behavior of zircaloy-4, Nucl. Instr. Meth. Phys. B 434 (2018) 81–87.
[7] L. Chai, S. Wang, H. Wu, Z. Yang, H. Pan, B. Song, N. Guo, Bimodal plate structures induced by pulsed laser in duplex-phase Zr alloy, Sci. China Technol. Sci. 60 (2017) 587–592.
[8] Y. Jung, H. Kim, I. Kim, S. Kim, J. Park, D. Park, J. Yang, Y. Koo, Strengthening of Zircaloy-4 using Y_2O_3 particles by a laser-beam-induced surface treatment process, Mater. Des. 116 (2017) 325–330.
[9] W. Bao, J. Xue, J. Liu, X. Wang, Y. Gu, F. Xu, G. Zhang, Coating SiC on Zircaloy-4 by magnetron sputtering at room temperature, J. Alloy. Comp. 730 (2018) 81–87.
[10] J. Yang, X. Wang, Q. Wen, X. Wang, R. Wang, Y. Zhang, W. Xue, The effect of microarc oxidation and excimer laser processing on the microstructure and corrosion resistance of Zr–1Nb alloy, J. Nucl. Mater. 467 (2015) 186–193.
[11] B. Cheng, Y. Kim, P. Chou, Improving accident tolerance of nuclear fuel with coated Mo-alloy cladding, Nucl. Eng. Technol. 48 (2016) 16–25.
[12] K. Amouzouvi, C. L, S. R, Microstructural changes in laser hardened Zr-2.5 Nb alloy, Scripta Metall. Mater. 2 (1995) 289–294.
[13] L. Chai, H. Wu, S. Wang, K. Chen, T. Wang, J. Xia, Characterization of microstructure and hardness of a Zr-2.5Nb alloy surface-treated by pulsed laser, Mater. Chem. Phys. 198 (2017) 303–309.
[14] L. Chai, B. Chen, S. Wang, N. Guo, C. Huang, Z. Zhou, W. Huang, Microstructural changes of Zr702 induced by pulsed laser surface treatment, Appl. Surf. Sci. 364 (2016) 61–68.
[15] L. Chai, B. Chen, S. Wang, Z. Zhou, W. Huang, Microstructural characteristics of

a commercially pure Zr treated by pulsed laser at different powers, Mater. Char. 110 (2015) 25–32.
[16] L. Chai, S. Wang, H. Wu, N. Guo, H. Pan, L. Chen, K.L. Murty, B. Song, α→β Transformation characteristics revealed by pulsed laser-induced non-equilibrium microstructures in duplex-phase Zr alloy, Sci. China Technol. Sci. 60 (2017) 1255–1262.
[17] S. Lee, C. Park, Y. Lim, H. Kwon, Influences of laser surface alloying with niobium (Nb) on the corrosion resistance of Zircaloy-4, J. Nucl. Mater. 321 (2003) 177–183.
[18] L.J. Zhang, H.Y. Fan, H. Wu, S.H. Ying, C.C. Zhou, C. Li, Microstructures and properties of Zr-4 alloy treated by surface niobium alloying, Heat Treat. Met. 32 (2007) 72–74.
[19] L.H. Keys, G. Johanson, A.S. Malin, The physical metallurgy of high strength zirconium alloys, J. Nucl. Mater. 59 (1976) 137–148.
[20] Y.I. Jung, Y.N. Seol, B.K. Choi, J.Y. Park, Y.H. Jeong, Effect of Cr on the creep properties of zirconium alloys, J. Nucl. Mater. 396 (2010) 303–306.
[21] B.X. Zhou, M.Y. Yao, Z.K. Li, X.M. Wang, J. Zhou, C.S. Long, Q. Liu, B.F. Luan, Optimization of N18 zirconium alloy for fuel cladding of water reactors, J. Mater. Sci. Technol. 28 (2012) 606–613.
[22] L. Chai, B. Luan, D. Xiao, M. Zhang, K.L. Murty, Q. Liu, Microstructural and textural evolution of commercially pure Zr sheet rolled at room and liquid nitrogen temperatures, Mater. Des. 85 (2015) 296–308.
[23] H.L. Yang, Y. Matsukawa, S. Kano, Z.G. Duan, K. Murakami, H. Abe, Investigation on microstructural evolution and hardening mechanism in dilute Zr–Nb binary alloys, J. Nucl. Mater. 481 (2016) 117–124.
[24] Y. Chi, G. Gu, H. Yu, C. Chen, Laser surface alloying on aluminum and its alloys: a review, Optic Laser. Eng. 100 (2018) 23–37.
[25] S. Banerjee, G.K. Dey, D. Srivastava, S. Ranganathan, Plate-shaped transformation products in zirconium-base alloys, Metall. Mater. Trans. 28 (1997) 2201–2216.
[26] W.G. Burgers, On the process of transition of the cubic-body-centered modification into the hexagonal-close-packed modification of zirconium, Physica 1 (1934) 561–586.
[27] L. Chai, B. Luan, M. Zhang, K.L. Murty, Q. Liu, Experimental observation of 12 α variants inherited from one β grain in a Zr alloy, J. Nucl. Mater. 440 (2013) 377–381.
[28] Y.B. Chun, M. Battaini, C.H.J. Davies, S.K. Hwang, Distribution characteristics of in-grain misorientation axes in cold-rolled commercially pure titanium and their correlation with active slip modes, Metall. Mater. Trans. 41 (2010) 3473–3487.
[29] D. Arias, J.P. Abriata, The Cr–Zr (Chromium-Zirconium) system, Bull. Alloy Phase Diagr. 7 (1986) 237–244.
[30] H.L. Yang, J. Shen, Y. Matsukawa, Y. Satoh, S. Kano, Z. Zhao, Y. Li, F. Li, H. Abe, Effects of alloying elements (Sn, Nb, Cr, and Mo) on the microstructure and mechanical properties of zirconium alloys, J. Nucl. Sci. Technol. 52 (2015) 1162–1173.
[31] B. Chen, L. Chai, S. Wang, N. Guo, B. Song, Z. Zhou, C. Huang, Investigation of microstructures of laser surface-treated Zr702 sheet using electron channeling contrast imaging and electron backscatter diffraction techniques, Surf. Coating. Technol. 296 (2016) 13–19.
[32] L. Chai, K. Chen, Y. Zhi, K.L. Murty, L. Chen, Z. Yang, Nanotwins induced by pulsed laser and their hardening effect in a Zr alloy, J. Alloy. Comp. 748 (2018) 163–170.